Planetary and Space Science 159 (2018) 56–65

Contents lists available at ScienceDirect

Planetary and Space Science

journal homepage: www.elsevier.com/locate/pss

The Multi-Temporal Database of Planetary Image Data (MUTED): A web-based tool for studying dynamic Mars

T. Heyer [a,*], H. Hiesinger [a], D. Reiss [a], G. Erkeling [b], H. Bernhardt [a], D. Luesebrink [a], R. Jaumann [c]

[a] Institut für Planetologie, Westfälische Wilhelms-Universität, Wilhelm-Klemm-Str. 10, 48149, Münster, Germany
[b] German National Library of Science and Technology (TIB), Hannover, Germany
[c] German Aerospace Center (DLR), Berlin, Germany

ARTICLE INFO

Keywords:
Database
Surface changes
Surface processes
Mars
Temporal analysis

ABSTRACT

Multi-temporal spacecraft observations are key to detect and understand surface changes and time-critical processes on Mars. Since the 1970s, the number of orbital observations of Mars has increased to over one million images. The observations have revealed that the surface of Mars is changing due to exogenic processes, including eolian activity, mass movement, seasonal ice and frost cover, and crater-forming impacts. The increasing number of observations highlights the importance of efficient and convenient tools for planetary image data management and change detection analyses. To support the identification of surface changes we developed the Multi-Temporal Database of Planetary Image Data (MUTED), which is accessible at "http://muted.wwu.de". The database enables scientists to quickly identify the spatial and multi-temporal coverage of planetary image data from Mars. As a basis for various change detection analyses, the location, number, and time range of acquisitions of overlapping images taken by the Viking Orbiter (VO), the Mars Orbiter Camera (MOC), the High Resolution Stereo Camera (HRSC), the Thermal Emission Imaging Instrument (THEMIS), the High Resolution Imaging Science Experiment (HiRISE), the Compact Reconnaissance Imaging Spectrometer of Mars (CRISM) and the Context Camera (CTX) as well as future instruments (e.g., Colour and Stereo Surface Imaging System (CaSSIS)) can be identified. The database will assist and optimize image data searches to support the analysis and understanding of short-term, seasonal, and long-term processes at the surface and in the atmosphere of Mars. To demonstrate the capability and scientific potential of the database, we analyzed the occurrence of dark slope streaks and observed their formation within a time interval of <~5 days in different regions on Mars.

1. Introduction

In the 1970s, the Mariner and Viking Orbiters provided about 55,000 images of the surface of Mars with a spatial resolution varying from a few meters to several hundreds of meters (Carr et al., 1972; Levinthal et al., 1973). Almost 25 years after the Viking program, observation systems on board of the Mars Global Surveyor (MGS), Mars Express (MEX), Mars Odyssey (MO) and the Mars Reconnaissance Orbiter (MRO) acquired images of the surface of Mars with a wide range of spatial and spectral resolutions, and different acquisition geometries. The observations have revealed that the martian surface is very dynamic (e.g., Sagan et al., 1972; Veverka et al., 1974; Chaikin et al., 1981; Zurek and Martin, 1993; Sullivan et al., 2001; Geissler, 2005; van Gasselt et al., 2005; Malin et al., 2006, 2010; Russell et al., 2008; Hayward et al., 2014; Raack et al., 2015; Vincendon et al., 2015). The modifications are attributed to exogenic processes, including eolian activity (e.g., Cantor et al., 2001; Bourke et al., 2008; Stanzel et al., 2006, 2008; Greeley et al., 2010; Reiss et al., 2011, 2014a; b; Reiss and Lorenz, 2016; Bridges et al., 2012, 2013; Daubar et al., 2016; Bennett et al., 2017), mass movement (e.g., Malin et al., 2006; Reiss et al., 2010; McEwen et al., 2011; Dundas et al., 2012, 2015; Ojha et al., 2015), seasonal ice and frost cover (e.g., James et al., 1979, 2010; Piqueux and Christensen, 2008; Thomas et al., 2009; Piqueux et al., 2015; Calvin et al., 2017), and crater-forming impacts (e.g., Malin et al., 2006; Daubar et al., 2013). Multi-temporal observations are key to detect and understand surface changes and processes on Mars. Since the Mariner and Viking program, the overall number of image data has risen to over one million (Heyer et al., 2017). The present status of the growing number of high-resolution observations with a spatial size of imaging pixels on the ground better than 100 m (m/px) and advantages of multi-temporal imaging is reported for example by

* Corresponding author.
E-mail address: thomas.heyer@uni-muenster.de (T. Heyer).

https://doi.org/10.1016/j.pss.2018.04.015
Received 30 October 2017; Received in revised form 6 March 2018; Accepted 14 April 2018
Available online 18 April 2018

Sidiropoulos and Muller (2015). Moreover, the increasing number of observations highlights the importance of efficient and convenient tools for planetary image data management and change detection analyses, which is what the Multi-Temporal Database of Planetary Image Data (MUTED) was developed for. The database enables scientists to quickly identify the spatial and multi-temporal coverage of Mars orbital image data. As a basis for various change detection analysis, the location, number, and time range of acquisitions of overlapping images taken by instruments on board of Viking, MO, MGS, MEX, and MRO can be identified with MUTED. In particular, images of the surface of Mars can be searched in spatial and temporal relation to other images. The temporal relation can be defined by the user in minutes, hours, days or a difference in solar longitude. The database will assist and optimize image data searches to support the analysis and understanding of short-term, seasonal, and long-term processes on the surface and in the atmosphere of Mars.

In this article, we present the current status of MUTED. A detailed description of the architecture and user interface of the database is presented in Section 2. The integrated datasets are briefly introduced in Section 3. Section 4 provides a global statistical analysis of the multi-temporal image coverage of the surface of Mars. The benefits of MUTED and a scientific case study of analyzing the temporal characteristics of dark slope streaks are discussed in Section 5.

2. The Multi-Temporal Database of Planetary Image Data

The Multi-Temporal Database of Planetary Image Data (MUTED) has been designed to support the identification of multi-temporal image coverage on Mars. The database has been developed at the Institut für Planetologie in Münster (IfP) and is available at URL: "http://muted.wwu.de". A comprehensive overview of application possibilities of multi-temporal observations on Mars as well as a simple implementation of the multi-temporal search algorithm has already been presented to the planetary community by Erkeling et al. (2016). Here, we present a detailed description of the implementation of the new developed multi-temporal search algorithm as a part of a comprehensive web-tool to study dynamic Mars.

MUTED was built using free and open source software and provides coverage information for more than one million images from several instruments imaging Mars. Its capabilities have already been utilized by some recent studies on active processes on the surface and in the atmosphere of Mars (Reiss et al., 2011; Jaumann et al., 2015).

The multi-temporal database is based on a three-tier architecture, including a data storage level, a service level, and a presentation level. Fig. 1 illustrates the architecture of MUTED and the corresponding data sources.

At the bottom data storage level, metadata of all images are stored within an object-relational database. Furthermore the temporal relations of all images are computed. For this purpose, we use a PostgreSQL database in combination with the PostGIS geospatial extension.

Metadata of the planetary image datasets are integrated from the Planetary Data System (PDS, https://pds.nasa.gov) of the National Aeronautics and Space Administration (NASA). For HRSC image data, the metadata are directly provided by the mission team at the German Aerospace Center (DLR). Product IDs, acquisition times, pixel resolutions, incidence angles, link to PDS, link to browse images, and the spatial extent of the images were extracted, unified, and stored in separate tables. Based on the spatial accuracy of the datasets, the spatial extent of the images diverges from the actual mapped area by an offset that may reach up to several hundred meters. Consequently, the spatial accuracy of the multi-temporal coverage results from the positional accuracy of the underlying images.

Datasets were filtered for data gaps and additional information, e.g., the Unix timestamp, the solar longitude, are derived for each image respectively. The Unix timestamps, which represents the number of seconds that have passed since the beginning of 1970-01-01 00:00:00

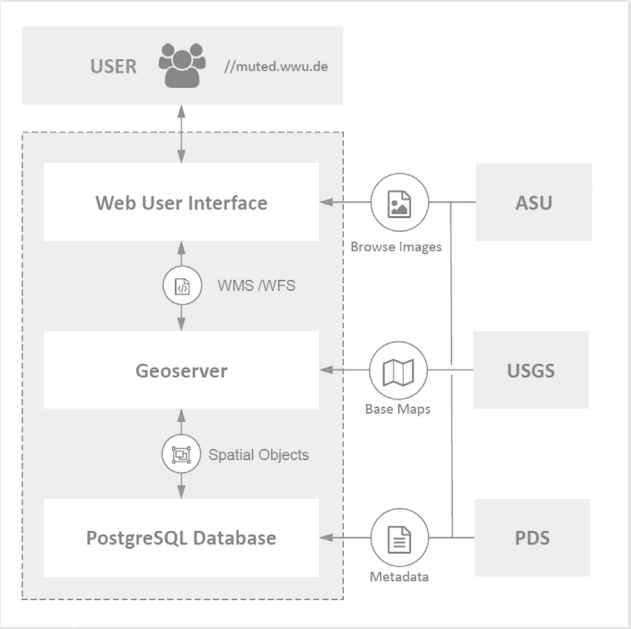

Fig. 1. Architecture of MUTED (dashed frame) and corresponding data sources.

UTC, are used to accelerate temporal database queries as well as the calculation of time intervals between overlapping images. To provide the temporal relation between overlapping images, time-overlap tables were created for each dataset respectively. Using the PostGIS spatial intersection algorithm, overlapping image objects were identified and the difference in time and solar longitude, and the number of overlapping images were stored for each image respectively. The overall number of overlapping footprints per image depends on the extent and location of the images and can be several magnitudes higher than the number of images integrated into the database. Due to storage capacity, the difference in time and solar longitude are only stored for the temporally nearest overlapping images. This value is used to provide the location of overlapping images for a user defined time range at a global scale. For a region of interest, all overlapping images can be identified on the fly using multi-temporal filter functions from the service level.

The service level of the database architecture comprises a Geoserver for data management and access. Using standards from the Open Geospatial Consortium (OGC), the Geoserver translates geospatial data, stored in the PostGreSQL database, into web map services (WMS) and web feature services (WFS). The WMS provides a global rasterized representation of image coverage. For a region of interest, WFS provides selectable vector representation of the images. Using Common Query Language (CQL), the web services can be filtered by date, solar longitude, spatial resolution, incidence angle and spatial extend.

In addition to the image datasets stored in the database, global basemaps provided by the United States Geological Survey (USGS) are integrated into the Geoserver and translated to WMS. A GeoWebCache is used to cache map tiles and accelerate as well as optimize the WMS delivery.

The presentation layer is a web user interface. Using HTML, PhP, and JavaScript, it provides several features for data selection, filtering and visualization (Fig. 2). A short user manual introduces all major elements and features of the user interface when accessing the website. Global basemaps can be selected within the navigation menu. Global basemaps provide a quick overview and spatial context, and support the definition of a region of interest (ROI) based on spectral, topographical or geological information. A ROI can be specified by drawing a rectangle on the map. Alternatively, the ROI can be set by minimum and maximum latitude and longitude coordinates. To visualize the data coverage for a specific instrument, all integrated datasets and further information are

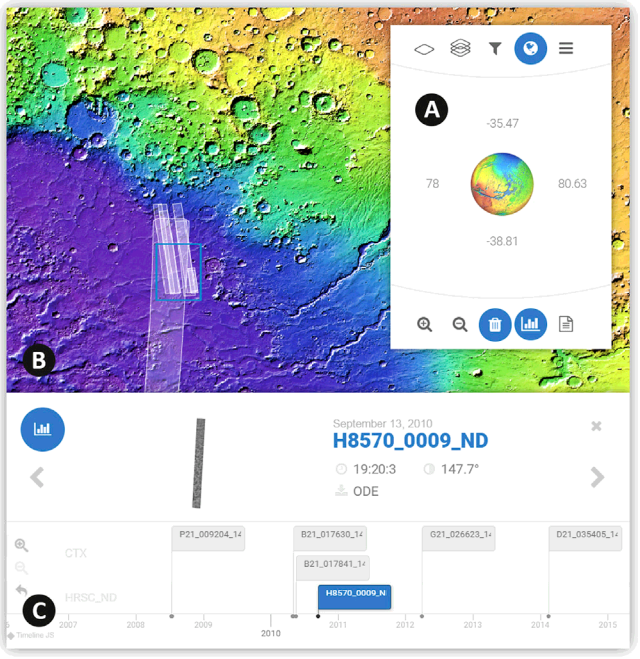

Fig. 2. Web user interface of MUTED. (A) Navigation menu. (B) Map area shows multi-temporal coverage on a global scale or for a region of interest (blue frame) on top of a selected basemap. (C) Timeline represents data availability and temporal context of all images within the region of interest in chronological order. (For interpretation of the references to color in this figure legend, the reader is referred to the Web version of this article.)

listed and can be selected in the dataset menu. Within the filter menu, datasets can be filtered by minimum and maximum thresholds for pixel resolution, date, solar longitude, or incidence angle.

By selecting datasets, a CQL-request consisting of the name of the dataset and the spatial and temporal thresholds is transmitted to the Geoserver. The Geoserver returns the spatial coverage of the requested dataset as WMS or WFS (ROI), including meta data stored in the PostgreSQL database.

By selecting images within the ROI, metadata and a browse image are displayed. Browse images are provided by the PDS and the Image Explorer from Arizona State University. Another feature of the user interface is a timeline that displays all selected images in chronological order. The timeline serves as a quick overview of the data availability and visualizes the temporal context of the images within the ROI.

The key feature is the multi-temporal search function. Overlapping images can be identified by selecting two or more datasets and a temporal relationship between the images. For the observation of short-term processes, the temporal relation can be set to minutes, hours or days. To observe seasonal processes, a difference in solar longitude can be defined. Alternatively, a minimum number of observations can be set to ensure data availability, e.g., to observe long-term processes.

By using the multi-temporal search function, a CQL-request consisting of the selected datasets and the temporal relationship is transmitted to the Geoserver. Based on the first selected dataset, the Geoserver returns the spatial coverage of the equivalent time-overlap table filtered by the minimum temporal difference to the second selected dataset. On the map (Fig. 3), red-colored objects indicate at least one image overlap for the defined temporal condition. By selecting the red-colored objects, another CQL-request consisting of the overlap dataset, the temporal relationship, and the spatial extend of the selected object is transmitted to the Geoserver. The resulting WFS represents the full overlap for the selected image.

A demonstration of the multi-temporal search function is presented in Fig. 3, showing overlapping observations from the High Resolution Stereo Camera (HRSC) and the Mars Orbiter Camera (MOC) within a time interval of 1 h. By selecting the identified HRSC images (red-colored objects), a CQL-request consisting of the overlap dataset name, the temporal thresholds (acquisition time plus and minus 1 h), and the spatial extend of the HRSC image is transmitted to the Geoserver. Overlapping MOC images (white-colored objects) including metadata and browse images appear on the map. This approach allows for a quick and convenient recognition of spatial and temporal overlaps among various datasets and has already been applied for scientific studies. For example, within the presented images, Reiss et al. (2011) observed active dust devils and analyzed their size, traverse velocities, and the direction of motion.

An example focusing on the multi-temporal data availability is presented in Fig. 4. The example shows images taken by the Context Camera (CTX) with more than 20 overlapping CTX observations and reveals suitable areas for extensive surface change analysis. In order to observe seasonal phenomena, the identified images can be further filtered by solar longitude or a specific time range.

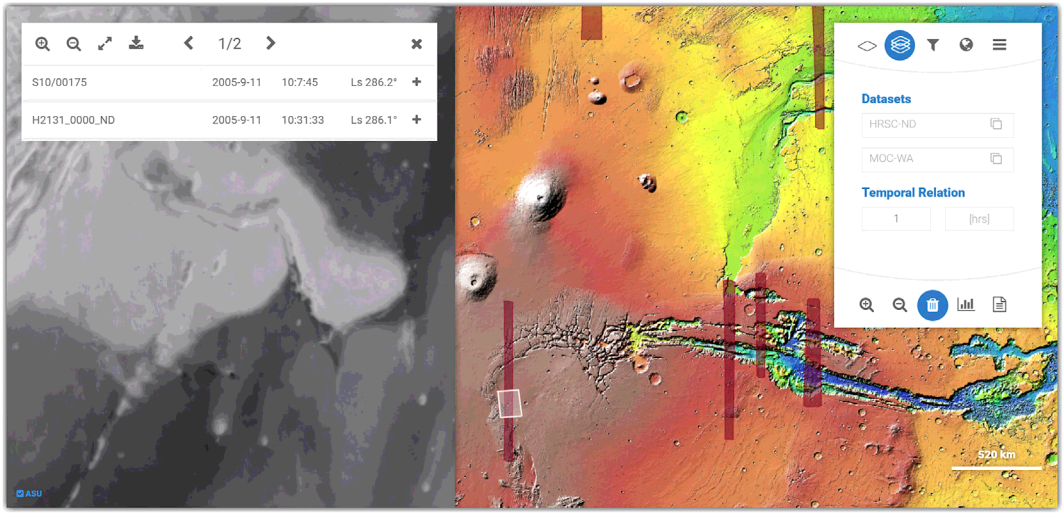

Fig. 3. Multi-temporal coverage of HRSC (red-colored objects) and MOC (white-colored objects) observations within a time interval of 1 h (right). Metadata and preview of the selected image (left). (For interpretation of the references to color in this figure legend, the reader is referred to the Web version of this article.)

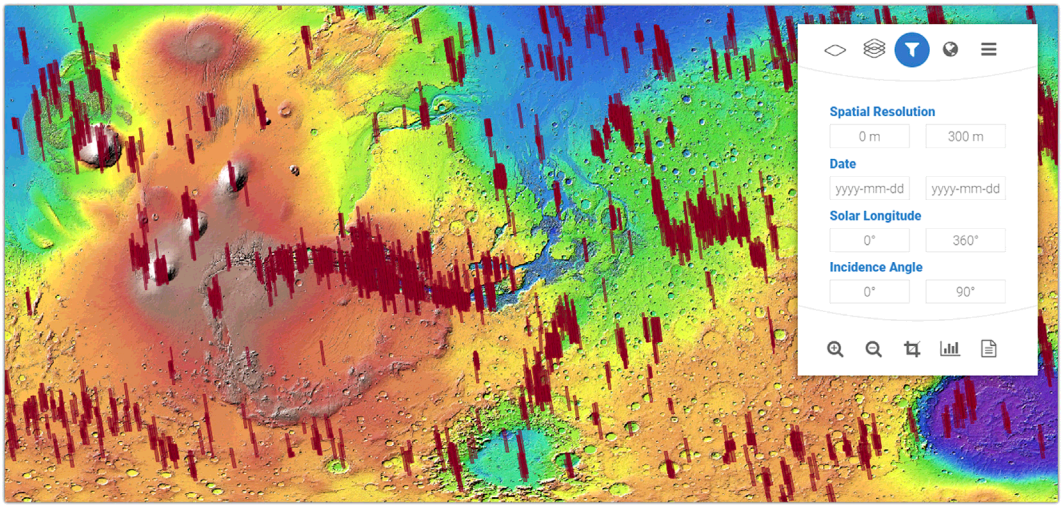

Fig. 4. The multi-temporal coverage of overlapping CTX images (>20 images) and available filter options.

3. Datasets

Currently, metadata pertaining to more than 1.27 million images taken by instruments on board of Viking, MO, MGS, MEX, and MRO are integrated into the database. Image data cover a time range of four decades beginning with the first image taken by the Viking Orbiter in 1976. The spatial resolution of the image data ranges from ~25 cm to several kilometers per pixel.

A first comprehensive view of the surface of Mars was achieved by the two Viking Orbiters (Carr et al., 1972). The orbiters reached Mars ~50 days apart at the end of northern spring of Mars Year 12 (1976) (Soffen and Snyder, 1976). In the following two and a half martian years more than 47,000 images with a spatial resolution between seven and several hundred meters per pixel were collected. On this basis, the first global mosaic of Mars with a pixel resolution of 231 m at the equator was created (Kirk et al., 1999; Archinal et al., 2003). Half of the images taken by the Viking Orbiter have a spatial resolution of 100 m/px and better. The 5804 high-resolution images with a spatial resolution of 25 m/px and better represent a valuable basis for surface change investigations over the last 22 martian years or 44 Earth years.

Almost ten martian years after the Viking program, Mars Global Surveyor (MGS) arrived at the end of northern summer of Mars Year 23 (1997) (Malin et al., 1992; Malin and Edgett, 2001). Using two camera systems, more than 360,000 images were acquired over the following five martian years. Focusing on seasonal phenomena in the atmosphere and on the surface of Mars, the Mars Orbiter Camera Wide Angle (MOC-WA) acquired images at a spatial resolution of 240 m/px to 7.5 km/px. The Mars Orbiter Camera Narrow Angle (MOC-NA) achieved a global coverage of 5.45% with high-resolution images at a spatial resolution of 1.5–12 m/px (Malin et al., 1992, 2010).

Mars Odyssey (MO) entered the martian orbit during northern fall of Mars Year 25 (2001). MO is still active and the longest surviving orbiter in Mars exploration. Its Thermal Emission Imaging Instrument (THEMIS) consist of two instruments observing the surface of Mars at the visible and near-infrared part of the spectrum (Christensen et al., 2004). The THEMIS-VIS camera acquires images with a spatial resolution of 18 m/px and covered more than 60% of the planet after eight martian years of operation. Infrared images from the THEMIS-IR spectrometer are typically more than 600 km long and cover a wavelength range of 6.7–14.8 µm at a spatial resolution of 100 m/px (Christensen et al., 2004). Using infrared observations, Edwards et al. (2011) produced a global day- and nighttime mosaic with a spatial resolution of ~100 m/px at the equator.

ESA's Mars Express (MEX) reached Mars during northern winter of Mars Year 26 (2003). The High Resolution Stereo Camera (HRSC) on board of MEX images the surface of Mars in four colors and five different phase angles (up to 18.9°) at a spatial resolution of 12.5 m/px. This configuration allows the derivation of digital terrain models with a grid size of up to 50 m and a height accuracy of 10 m. Due to the elliptical orbit, the spatial resolution depends on the respective distance from the surface of Mars (Neukum and Jaumann, 2004; Jaumann et al., 2007; Gwinner et al., 2016). After ten Earth years of operation, ~70% of the surface are covered by panchromatic images with a spatial resolution better than 20 m/px and ~90% with a spatial resolution better than 100 m/px (Gwinner et al., 2016).

At northern spring of Mars Year 28 (2005), after five months of aerobraking, the Mars Reconnaissance Orbiter (MRO) entered its final orbit around Mars. MRO has three optical instruments to characterize the geology and mineralogy of the surface of Mars at high spatial and spectral resolution. The currently highest available orbital image resolution of 0.25–0.5 m/px is achieved by the High Resolution Imaging Science Experiment (HiRISE) (McEwen et al., 2007). Focusing on detailed geomorphology and stratigraphy of key locales, high-resolution images cover 2.4% of the martian surface after five martian years of operation. The Context Camera (CTX) acquires 30 km wide and more than 40 km long context images with a spatial resolution of 5–6.5 m/px (Malin et al., 2007). Due to the large areal coverage, in early 2017, 99% of the planet is covered after almost six martian years of operation. High-resolution spectral observations are provided by the Compact Reconnaissance Imaging Spectrometer of Mars (CRISM) operated in three observing modes. In multispectral mapping mode, a subset of data is collected at 72 wavelengths with a spatial resolution of 100 and 200 m/px. After five martian years of operation, observations cover more than 80% of surface of Mars at multiple visible and infrared parts of the spectrum. In targeted mode, images at a spectral range from 362 nm to 3920 nm (6.55 nm/channel) with a spatial resolution of 20 m/px are acquired (Murchie et al., 2007). Currently, images taken in the atmospheric mode are not integrated in the database. Table 1 summarizes the quantitative, spatial, and temporal characteristics of the integrated datasets.

In addition to the image datasets, five global basemaps are integrated into MUTED. An overview of Mars at visible wavelengths is provided by the Viking MDIM2.1 Colorized Global Mosaic with a spatial resolution of ~231 m/px at the equator (Archinal et al., 2003). A more detailed view with a spatial resolution of ~100 m/px at mid-infrared wavelengths is available from the THEMIS-IR day-time global mosaic. In addition, the THEMIS-IR night-time mosaic was included, which shows the thermal emissivity of the surface (Edwards et al., 2011). Topographic information is provided by a Mars Orbiter Laser Altimeter (MOLA) shaded relief

Table 1
All planetary image datasets integrated into MUTED.

Dataset	Time range (years)	Type	Spatial resolution (m/px)	Spectral range (nm)	Images
Viking	1976–1980		≥7	450–590	47015
MOC	1997–2006	NA	≥1.5	500–900	95425
		WA	≥230	400–675	140435
THEMIS	2002 ~	VIS	≥18	400–900	221455
		IR	≥100	6700–14800	208044
HRSC	2004 ~	ND	≥12.5	440–970	4153
		BL, GR, RE, IR, S1, S2, P1, P2	≥12.5		30921
CRISM	2006 ~	HRS, HRL, FRS, ATO, ATU	≥20	362–3920	210899
		MSW, HSV, HSP, MSV	≥100		133253
CTX	2006 ~		≥6	500–700	81581
HiRISE	2006 ~		≥0.25	350–900	96232

derived from altimetry colorized by elevation with a spatial resolution of ~463 m/px (Smith et al., 2001). Global geological information of the martian surface is available from the geological map of Tanaka et al. (2014).

4. Coverage analysis

In order to quantify the multi-temporal coverage of the integrated datasets we defined a latitude-longitude raster of Mars with a spatial resolution of 0.01° and applied a raster filling algorithm for all image footprints. The derived footprint raster is aggregated under different temporal and spatial constrains and transformed into an equal area map using the Mollweide projection. The spatial resolution of the global base raster is equal to 600 m at the equator of Mars. The swath width of the smallest integrated images is 2.9 km for MOC-NA (Malin et al., 1992) and 1.2 km for HiRISE (McEwen et al., 2007). In comparison to the final coverage of MOC-NA of 5.45%, reported in Malin et al. (2010), our estimate of 5.449% for the overall MOC-NA coverage confirms an adequate accuracy of our coverage analysis.

For the statistical analysis we included all images covering the visible part of spectrum that are both integrated in MUTED and published in PDS until August 2017. For the HRSC data set, the analysis focuses on the nadir (ND) images. Calibration images and images covering the two natural satellites of Mars, Phobos and Deimos, are excluded from the statistical analysis. In addition to an overall overview of the integrated datasets, the images were aggregated based on the spatial resolution: better than 25, 100, and 500 m/px (abbreviated below as high, medium, and low resolution).

Fig. 5 shows the global coverage per quarter Mars year starting from the first image taken by Viking in 1976 until present. In the last 10 Mars years (since MGS reached Mars), the surface of Mars is covered by ~98,000 images per Mars year with various spectral and spatial resolutions. For the same period, ~59,000 high-resolution images per Mars year were acquired. The mean annual coverage of high-resolution images is 26.4% of the surface of Mars.

Fig. 6 shows the global coverage as a function of solar longitude and thus as a function of season. In this plot, all images from Mars Year 12 until 34 are grouped in intervals spanning 30° in solar longitude (defined as one month on Mars). The average coverage of the surface of Mars per 30° interval for images with a spatial resolution better than 500 m/px is ~79% (~32% for high-resolution images). Northern spring is the longest season on Mars (~194 sols) and is ~40 sols longer in comparison to northern fall. As a result, spring months show the highest coverage with a maximum between 30° and 60° solar longitude for high- and medium-resolution images. In fall, we calculated a minimum coverage for high-resolution images of ~18% between 210° and 240° solar longitude. In addition to season length, observing conditions and data downlink capacity from orbiter to Earth affects image acquisition and seasonal coverage.

For a multi-temporal coverage analysis, all images from Mars Year 12 until 34 were aggregated. The overall repeat coverage of all high-to low-resolution images is presented in Fig. 7.

The multi-temporal analysis shows that images with a spatial resolution better than 500 m/px cover the surface of Mars completely (100%) up to five times. For half of the surface, at least 28 high-to low-resolution images are available. Polar regions are covered up to ~1200 times (Fig. 8). High-resolution images cover 99.9% of the surface of Mars. For 98.4% of the surface at least one pair of high-resolution observations is available. Half of the surface is covered with at least 5 high-resolution images. Areas with a maximum coverage of ~800 images are within the polar regions. Landing sites and other prominent areas are covered up to ~300 times. Figs. 8 and 9 show the global coverage of Mars with images better than 500 m/px and 25 m/px, respectively.

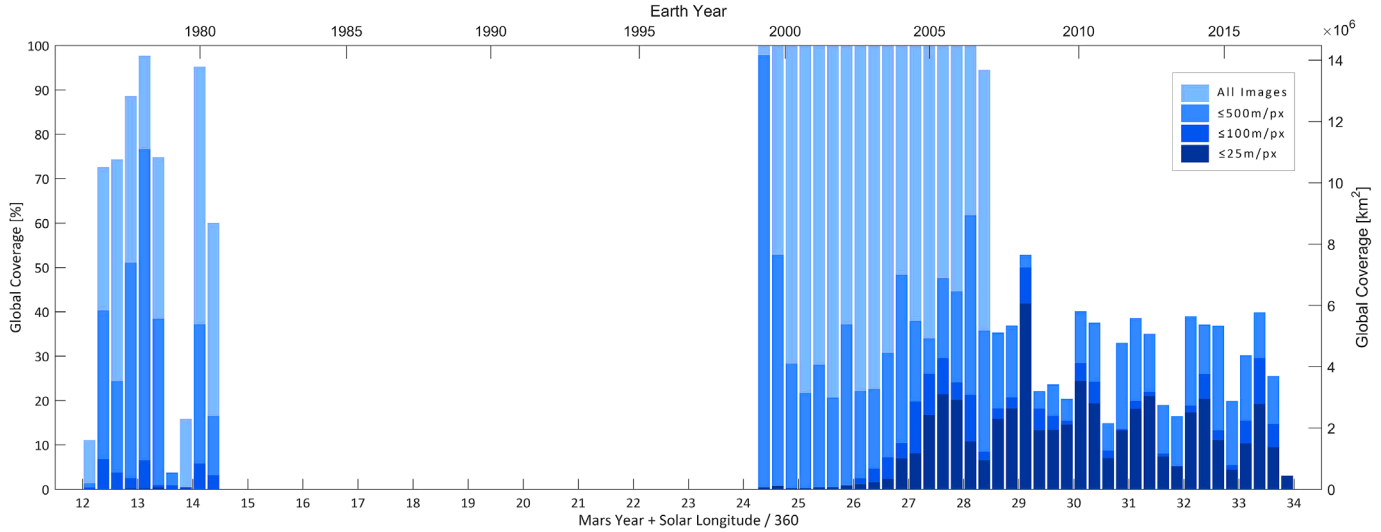

Fig. 5. Global coverage of all datasets integrated into MUTED per quarter Mars year. Coverage represents the area of the surface of Mars, which was observed at least one time during a quarter Mars year interval.

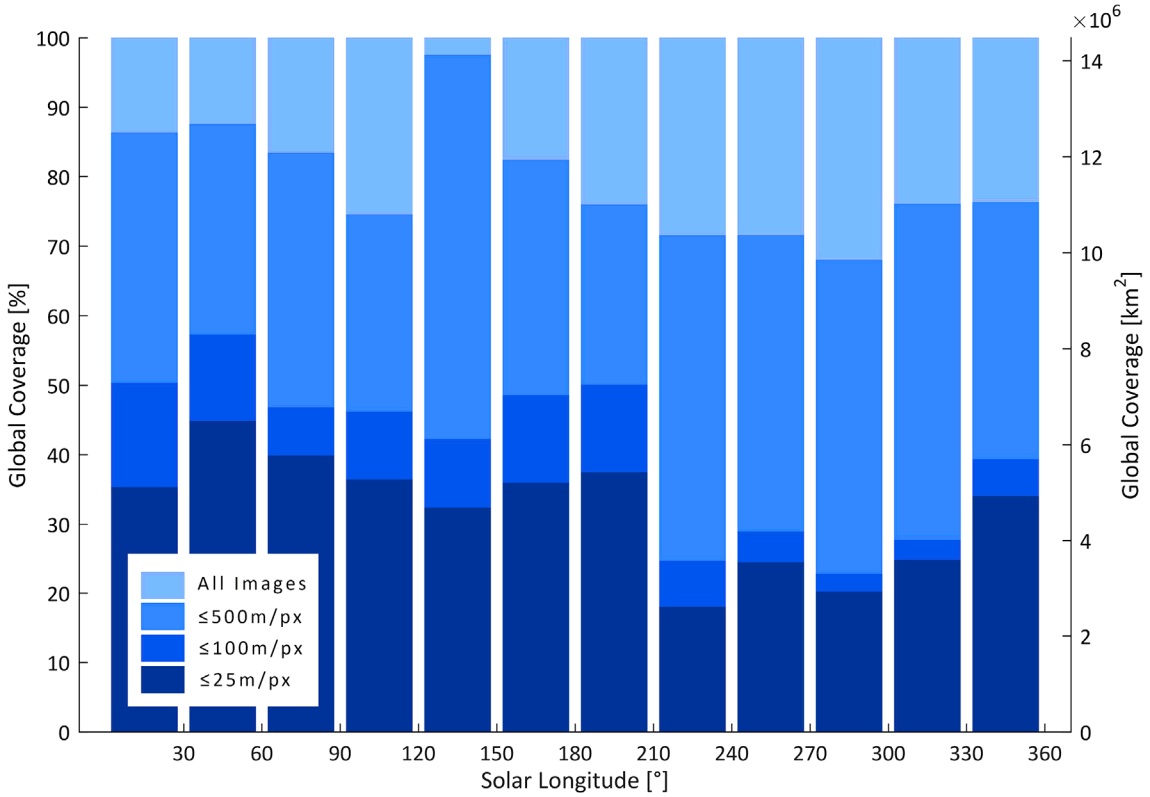

Fig. 6. Global coverage of all datasets integrated into MUTED per 30° in solar longitude. Coverage represents the area of surface of Mars, which was observed at least one time during a martian month.

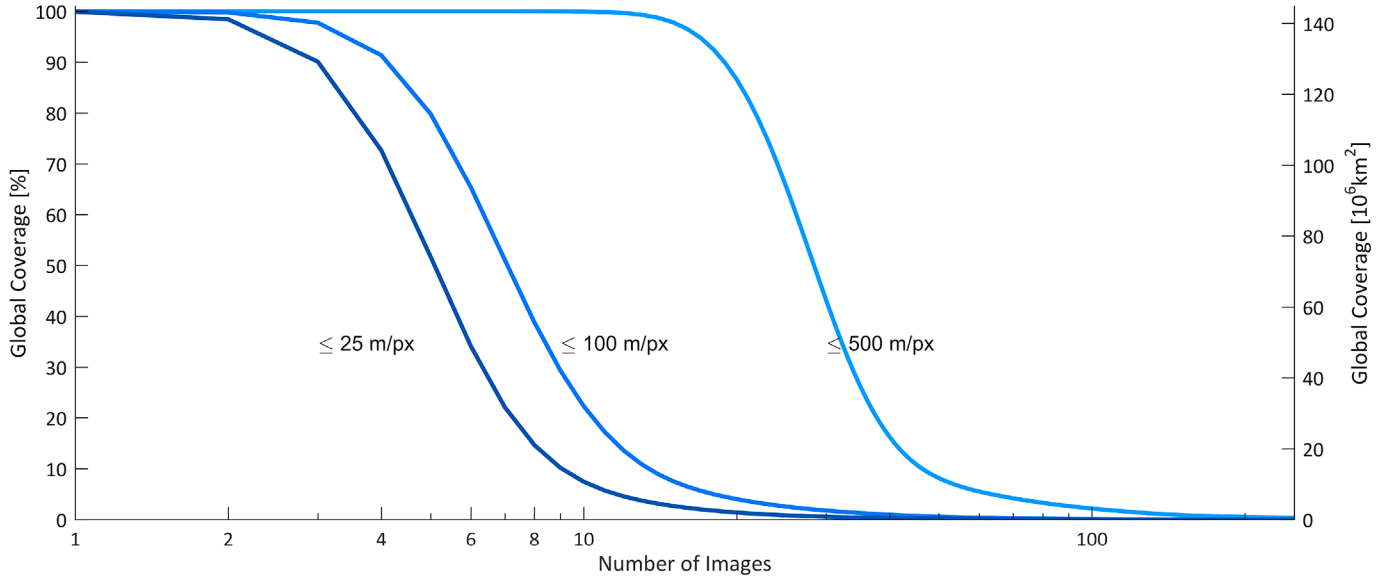

Fig. 7. Global repeat coverage of all datasets integrated into MUTED.

The multi-temporal coverage for high-to low-resolution images during different martian seasons is presented in Table 2. 88.7–99.0% of the surface of Mars is mapped more than once with high-to low-resolution images. Ten and more high-to low-resolution observations are available for 17.6–45.9% of the surface. 25.7–37.6% of the surface is covered by two and more high-resolution images. For 0.3–0.9% of the surface ten and more high-resolution images are available.

In summary, the seasonal multi-temporal coverage reveals an adequate data basis to detect and analyze time-critical phenomena and processes on the surface and in the atmosphere of Mars.

The multi-temporal analysis reveals a comprehensive data availability for various change detection investigations over the last ten Mars years. For example, the extensive multi-temporal coverage of the polar regions is a valuable resource to analyze seasonal variations of ice and frost cover and polar processes. The excellent coverage of regions with steep slopes (e.g., Valles Marineris) enables a comprehensive monitoring of mass-wasting processes. Due to the global multi-temporal coverage of high-resolution images, new impact craters can be detected at a global scale.

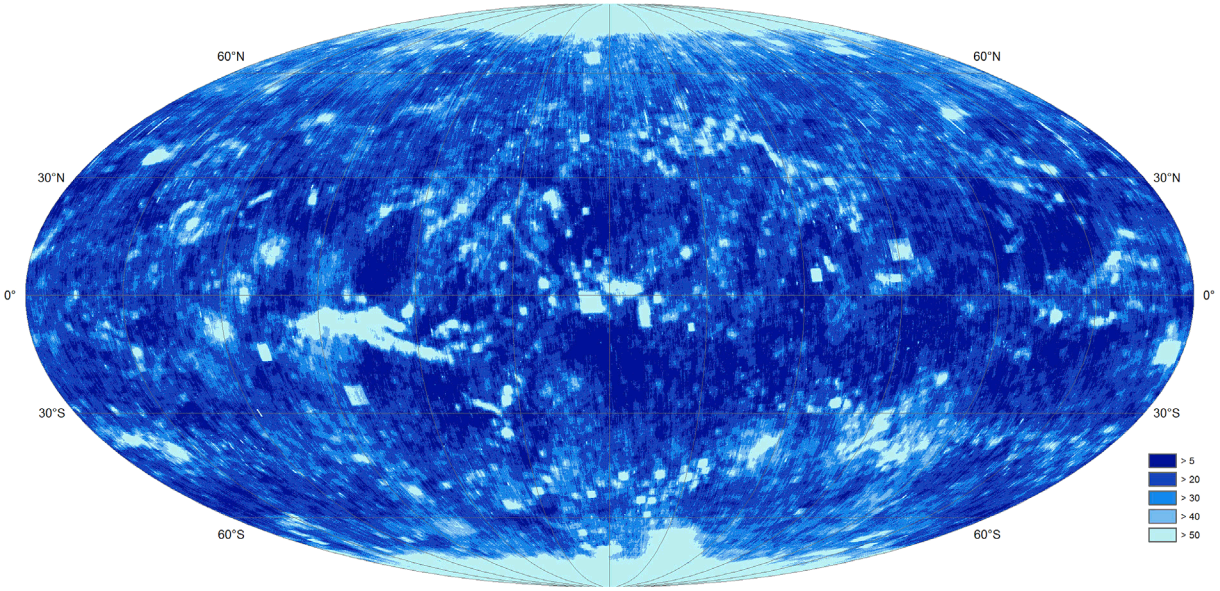

Fig. 8. Number of images with a spatial resolution better than 500 m/px per 0.01°.

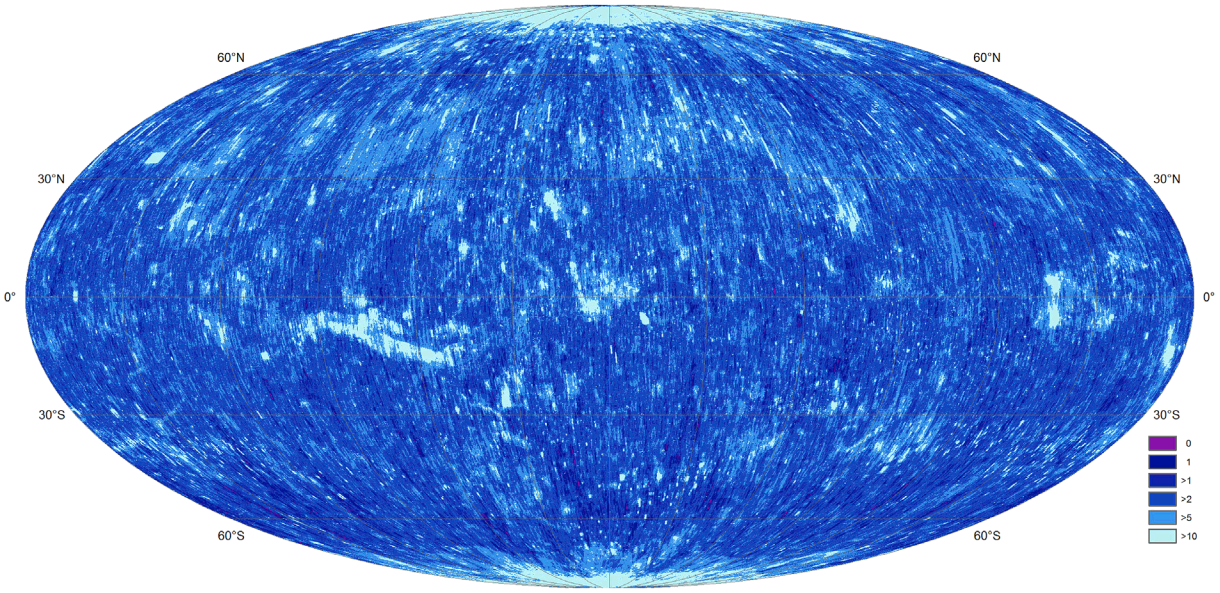

Fig. 9. Number of images per 0.01° with a spatial resolution better than 25 m/px.

Table 2
Global repeat coverage per Mars season starting from northern spring (1) to winter (4).

Number of images	Coverage [%] (≤25 m/px)				Coverage [%] (≤100 m/px)				Coverage [%] (≤500 m/px)			
	Season				Season				Season			
	1	2	3	4	1	2	3	4	1	2	3	4
1	76.6	69.6	60.5	57.2	86.1	80.9	71.4	62.2	99.8	99.5	96.9	96.5
2	47.3	37.6	26.7	25.7	64.7	54.5	39.3	31.2	99.0	98.5	88.7	89.3
3	24.1	17.7	10.0	11.0	42.2	33.1	18.8	15.1	96.8	96.9	75.9	79.2
4	11.3	8.4	4.0	5.1	25.4	19.5	9.1	8.0	92.1	94.1	60.9	67.6
5	5.6	4.4	1.9	2.8	15.1	11.7	4.9	4.8	84.5	89.4	46.4	56.0
10	0.9	0.9	0.3	0.5	2.6	2.3	0.9	1.4	32.3	45.9	10.5	17.6

5. Example application – slope streaks

The following scientific example demonstrates the capability and performance of MUTED to support the identification of surface changes on Mars. The example focuses on the formation of slope streaks on Mars. Based on the ability of MUTED to search through a vast amount of multi-temporal image coverage, image pairs with a minimum temporal interval could be identified on a global scale. The image pairs are used to identify newly formed slope streaks and constrain the duration of their formation.

Slope streaks are narrow fan-shaped albedo features that occur on steep slopes in high-albedo and low-thermal-inertia equatorial regions of Mars (Sullivan et al., 2001). The distinctive dark and much rarer bright features have a high contrast and sharp edges (unresolved at ~25 cm) to the surrounding surface. The length of the slope streaks varies from several kilometers down to the size of the image resolution. Slope streaks were originally observed in high-resolution images of the Viking Orbiters in 1977 (Morris, 1982; Ferguson and Lucchitta, 1984). Newly formed streaks, observed in MOC images, revealed that slope streaks are actively forming (Sullivan et al., 2001). A number of models have been proposed to explain the formation of slope streaks on Mars. Dry-based models include mass-wasting of dust, granular flows or avalanching of heterogeneous dust accumulation along slopes (Sullivan et al., 2001; Baratoux et al., 2006; Chuang et al., 2007). Wet-based models comprise brine flows, mixed water-dusts flows, groundwater or ground-wetting from salty liquids (e.g., Ferguson and Lucchitta, 1984; Ferris et al., 2002; Miyamoto et al., 2004; Head et al., 2007; Jaret and Clevy, 2007; Kreslavsky and Head, 2009; Mushkin et al., 2010). However, none of the proposed models account for all of the observed characteristics. Brusnikin et al. (2016) considered different physical processes resulting in a more or less similar streak pattern. A growth or a reactivation of an existing slope streak has not been observed yet. Therefore, the formation of slope streaks is considered as a single short-time event, while the duration of the formation event is unknown (Brusnikin et al., 2016; Bhardwaj et al., 2017). The observation of the formation process is limited by the intervals between repeat images. Comparing MOC images, Aharonson et al. (2003) identified newly formed slope streaks within an interval of 109 days. When MO, MEX, and MRO reached Mars, the availability of overlapping high-resolution images increased dramatically. Chuang et al. (2007) identified newly formed slope streaks using HiRISE images within a time interval of 23 days. Comparing images of CTX and THEMIS-VIS, Schorghofer and King (2011) found newly formed slope streaks within an interval of 22 days.

In this example we used MUTED to analyze and constrain the maximum duration of the formation of slope streaks.

Using the multi-temporal function of MUTED, overlapping CTX images were identified for a time interval starting from one day up to one week. For the high-albedo equatorial regions, where slope streaks occur, ~200 image pairs were identified. Using MUTED, image pairs with a very small area of overlap were easily detectable and excluded from further analysis. MUTED provided meta-data information for all image pairs including a link to PDS, from which the image raw data were obtained. Within the 40 visually analyzed image pairs, we found three newly formed slope streaks (Fig. 10).

The first newly formed slope streak was identified on the northern rim of Pasteur crater at 20.13°N and 24.16°E. The slope streak has a length of ~400 m and points in south direction. The slope streak occurred in Mars Year 29 at a solar longitude of ~289.5°. The time interval between the overlapping CTX images is six days.

The second slope streak occurred in the Olympus Mons Aureole at 31.93°N and 137.80°W. The cone-shaped slope streak spreads in a southeast direction over a distance of ~510 m. The slope streak occurred in Mars Year 33 at a solar longitude ~29.7°. The CTX observations are also six days apart.

The third slope streak was also identified in the Olympus Mons Aureole at 30.86°N and 140.51°W, at a distance of ~100 km to the second observed streak. The slope streak has a length of ~1080 m and spreads towards the west. The slope streak also occurred in Mars Year 33 at a solar longitude of ~31.6°. The time interval between the overlapping CTX images is five days and provides the shortest indication for the duration of the formation process of slope streaks on Mars. The physiographic settings of the three analyzed dark slope streaks are

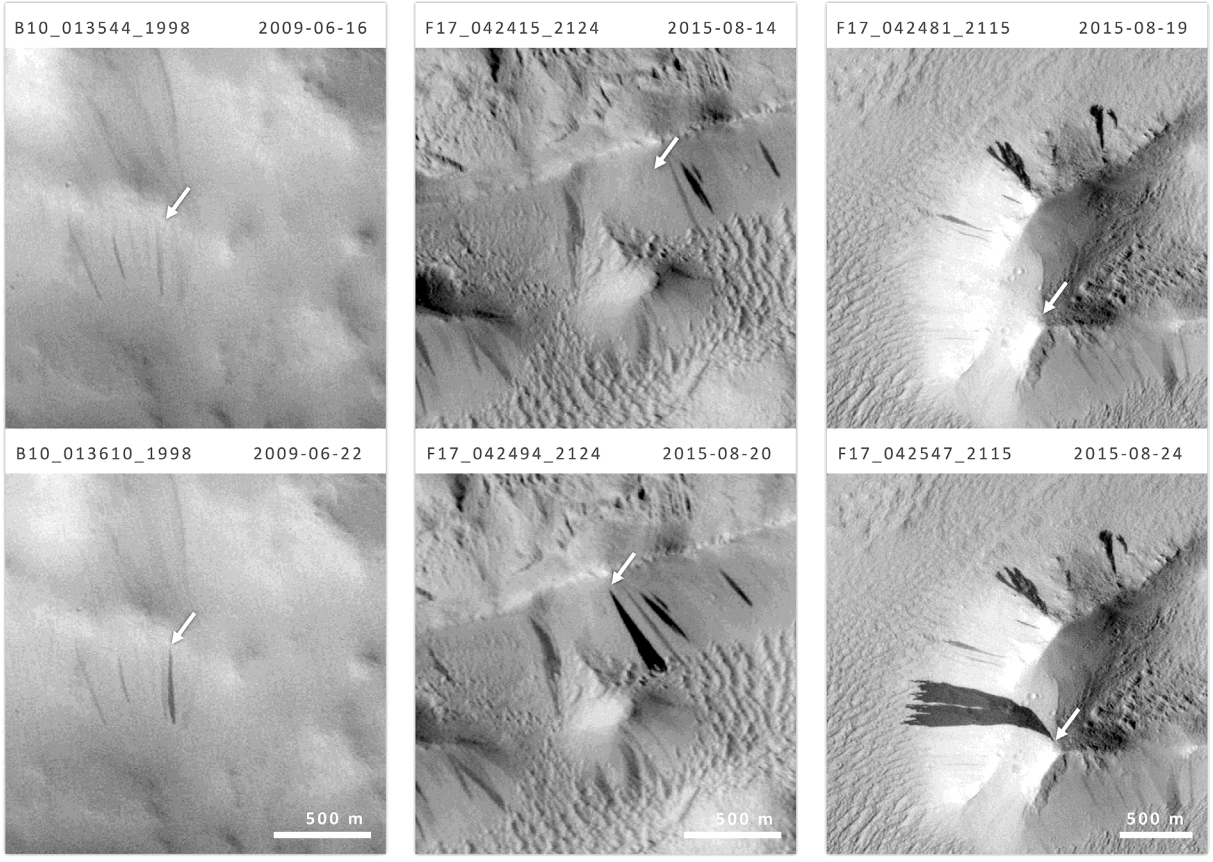

Fig. 10. Newly formed slope streaks within a time interval of five and six days on the northern rim of Pasteur crater (left) and in the Olympus Mons Aureole (middle and right). CTX images showing study sites before (top) and after (bottom) the formation of the slope streaks.

comparable to those investigated by Schorghofer and King (2011).

In summary, the observed slope streaks revealed a formation interval shorter than ~5 days. The temporal constraint of the formation process was observed in two different regions on Mars for slope streaks with a maximum length of ~400–~1000 m. The observed slope streaks occurred in martian spring as well as in winter. Our study is consistent with previous work (e.g., Schorghofer and King (2011)) and can be used to constrain the formation interval further. This type of analysis could be expanded to other multi-temporal studies on processes on the surface (e.g., gully erosion) and in the atmosphere (e.g., dust devils).

This example demonstrates the utility of multi-temporal analyses and provides new insights in the formation of slope streaks on Mars. It demonstrates the benefits of MUTED and its scientific potential and highlights the importance of a comprehensive and continuing monitoring of the surface of Mars.

6. Conclusion

MUTED represents a fast and convenient tool for identification of spatial and multi-temporal coverage of planetary image data and supports the identification of surface changes and processes on Mars. MUTED enables planetary scientists, engineers, and mission planners to identify more than 1.27 million observations from orbital instruments imaging the surface of Mars, including Viking, MOC, THEMIS, HRSC, HiRISE, CTX, and CRISM in spatial and temporal context. The statistical analysis of the integrated image datasets revealed a high availability of multi-temporal observations of the surface of Mars. 47% of the integrated images have a spatial resolution better than 25 m/px and cover 99.9% of the surface. Over the last ten Mars years almost 60,000 high-resolution images per Mars year were acquired. The increasing number of observations highlights the importance of efficient and convenient tools for planetary image data management and change detection analyses. The flexible architecture of MUTED allows for a fast integration of upcoming data sets, e.g., from India's Mars Orbiter Mission (MOM) or ESA's ExoMars Trace Gas Orbiter (TGO) mission. MUTED enables scientists to quickly identify the location, number, and time range of acquisitions of overlapping images on a global-scale or for a specific region of interest. It will assist and optimize image data searches to support the analysis and understanding of short-term, seasonal, and long-term processes on the surface and in the atmosphere of Mars. The example application provides new insights in the formation process of slope streaks and constrains the duration of the formation down to an interval of ~5 days. Furthermore, it shows the limitation of available observations of the surface of Mars and highlights the importance of continuing orbital monitoring.

Acknowledgements

We thank the HRSC Experiment Teams at DLR Berlin and Freie Universität Berlin as well as the Mars Express Project Teams at ESTEC and ESOC for their successful planning and acquisition of data as well as for making the processed data available to the HRSC Team. We acknowledge the effort of the HRSC Co-Investigator Team members and their associates who have contributed to this investigation in the preparatory phase and in scientific discussions within the team. We appreciate the constructive reviews provided by Matt Balme and an anonymous reviewer that significantly helped to improve the manuscript. This research has been funded and supported by the German Aerospace Agency (DLR) (Grant # 50QM1101 and 50QM1501).

References

Aharonson, O., Schorghofer, N., Gerstell, M.F., 2003. Slope streak formation and dust deposition rates on Mars. J. Geophys. Res. 108, 1–9. https://doi.org/10.1029/2003JE002123.

Archinal, B.A., Kirk, R.L., Duxbury, T.C., Lee, E.M., Sucharski, R., Cook, D., 2003. Mars Digital Image Model 2.1 Control Network. LPSC XXXIV #1485.

Baratoux, D., Mangold, N., Forget, F., Cord, A., Pinet, P., Daydou, Y., Jehl, A., Masson, P., Neukum, G., 2006. The role of the wind-transported dust in slope streaks activity: evidence from the HRSC data. The HRSC CO-Investigator Team Icarus 183, 30–45. https://doi.org/10.1016/j.icarus.2006.01.023.

Bennett, K.A., Fenton, L., Bell, J.F., 2017. The albedo of martian dunes: insights into aeolian activity and dust devil formation. Aeolian Res. 26, 89–100. https://doi.org/10.1016/j.aeolia.2016.08.009.

Bhardwaj, A., Sam, L., Martín-Torres, F.J., Zorzano, M.P., Fonseca, R.M., 2017. Martian slope streaks as plausible indicators of transient water activity. Sci. Rep. 7 https://doi.org/10.1038/s41598-017-07453-9.

Bourke, M.C., Edgett, K.S., Cantor, B.A., 2008. Recent aeolian dune change on Mars. Geomorphology 94, 247–255. https://doi.org/10.1016/j.geomorph.2007.05.012.

Bridges, N.T., Ayoub, F., Avouac, J.-P., Leprince, S., Lucas, A., Mattson, S., 2012. Earth-like sand fluxes on Mars. Nature 485, 339–342. https://doi.org/10.1038/nature11022.

Bridges, N., Geissler, P., Silvestro, S., Banks, M., 2013. Bedform migration on mars: current results and future plans. Aeolian Res. https://doi.org/10.1016/j.aeolia.2013.02.004.

Brusnikin, E.S., Kreslavsky, M.A., Zubarev, A.E., Patratiy, V.D., Krasilnikov, S.S., Head, J.W., Karachevtseva, I.P., 2016. Topographic measurements of slope streaks on Mars. Icarus 278, 52–61. https://doi.org/10.1016/j.icarus.2016.06.005.

Calvin, W.M., Cantor, B.A., James, P.B., 2017. Interannual and seasonal changes in the south seasonal polar cap of Mars: observations from MY 28-31 using MARCI. Icarus 292, 144–153. https://doi.org/10.1016/j.icarus.2017.01.010.

Cantor, B.A., James, P.B., Caplinger, M., Wolff, M.J., 2001. Martian dust storms: 1999 mars orbiter camera observations. J. Geophys. Res. Planets 106, 23653–23687. https://doi.org/10.1029/2000JE001310.

Carr, M.H., Baum, W.A., Briggs, G.A., Masursky, H., Wise, D.W., Montgomery, D.R., 1972. Imaging experiment: the viking mars orbiter. Icarus 16, 17–33.

Chaikin, A.L., Maxwell, T.A., El-Baz, F., 1981. Temporal changes in the cerberus region of mars: mariner 9 and viking comparisons. Icarus 45, 167–178. https://doi.org/10.1016/0019-1035(81)90012-9.

Christensen, P.R., Jakosky, B.M., Kieffer, H.H., Malin, M.C., McSween Jr., H.Y., Nealson, K., Mehall, G.L., Silverman, S.H., Ferry, S., Caplinger, M., Ravine, M., 2004. The thermal emission imaging system (THEMIS) for the mars 2001 Odyssey mission. Space Sci. Rev. 110, 85–130. https://doi.org/10.1023/B:SPAC.0000021008.16305.94.

Chuang, F.C., Beyer, R.A., McEwen, A.S., Thomson, B.J., 2007. HiRISE observations of slope streaks on Mars. Geophys. Res. Lett. 34 https://doi.org/10.1029/2007GL031111.

Daubar, I.J., Dundas, C.M., Byrne, S., Geissler, P., Bart, G.D., McEwen, A.S., Russell, P.S., Chojnacki, M., Golombek, M.P., 2016. Changes in blast zone albedo patterns around new martian impact craters. Icarus 267, 86–105. https://doi.org/10.1016/j.icarus.2015.11.032.

Daubar, I.J., McEwen, A.S., Byrne, S., Kennedy, M.R., Ivanov, B., 2013. The current martian cratering rate. Icarus 225, 506–516. https://doi.org/10.1016/j.icarus.2013.04.009.

Dundas, C.M., Diniega, S., Hansen, C.J., Byrne, S., McEwen, A.S., 2012. Seasonal activity and morphological changes in martian gullies. Icarus 220, 124–143. https://doi.org/10.1016/j.icarus.2012.04.005.

Dundas, C.M., Diniega, S., McEwen, A.S., 2015. Long-term monitoring of martian gully formation and evolution with MRO/HiRISE. Icarus 251, 244–263. https://doi.org/10.1016/j.icarus.2014.05.013.

Edwards, C.S., Nowicki, K.J., Christensen, P.R., Hill, J., Gorelick, N., Murray, K., 2011. Mosaicking of global planetary image datasets: 1. Techniques and data processing for Thermal Emission Imaging System (THEMIS) multi-spectral data. J. Geophys. Res. E Planets 116. https://doi.org/10.1029/2010JE003755.

Erkeling, G., Luesebrink, D., Hiesinger, H., Reiss, D., Heyer, T., Jaumann, R., 2016. The Multi-Temporal Database of Planetary Image Data (MUTED): a database to support the identification of surface changes and short-lived surface processes. Planet. Space Sci. 125, 43–61. https://doi.org/10.1016/j.pss.2016.03.002.

Ferguson, H.M., Lucchitta, B.K., 1984. Dark streaks on talus slopes. Mars. Planet. Geol. Geophys. Progr. Rep. 188–190.

Ferris, J.C., Dohm, J.M., Baker, V.R., Maddock III, T., 2002. Dark slope streaks on Mars: are aqueous processes involved? Geophys. Res. Lett. 29, 5–8. https://doi.org/10.1029/2002GL014936.

Geissler, P.E., 2005. Three decades of Martian surface changes. J. Geophys. Res. 110, 1–23. https://doi.org/10.1029/2004JE002345.

Greeley, R., Waller, D.A., Cabrol, N.A., Landis, G.A., Lemmon, M.T., Neakrase, L.D.V., Pendleton Hoffer, M., Thompson, S.D., Whelley, P.L., 2010. Gusev Crater, Mars: observations of three dust devil seasons. J. Geophys. Res. E Planets 115. https://doi.org/10.1029/2010JE003608.

Gwinner, K., Jaumann, R., Hauber, E., Hoffmann, H., Heipke, C., Oberst, J., Neukum, G., Ansan, V., Bostelmann, J., Dumke, A., Elgner, S., Erkeling, G., Fueten, F., Hiesinger, H., Hoekzema, N.M., Kersten, E., Loizeau, D., Matz, K.D., McGuire, P.C., Mertens, V., Michael, G., Pasewaldt, A., Pinet, P., Preusker, F., Reiss, D., Roatsch, T., Schmidt, R., Scholten, F., Spiegel, M., Stesky, R., Tirsch, D., Van Gasselt, S., Walter, S., Wählisch, M., Willner, K., 2016. The high resolution stereo camera (HRSC) of mars express and its approach to science analysis and mapping for mars and its satellites. Planet. Space Sci. 126, 93–138. https://doi.org/10.1016/j.pss.2016.02.014.

Hayward, R.K., Fenton, L.K., Titus, T.N., 2014. Mars global digital dune database (MGD3): global dune distribution and wind pattern observations. Icarus 230, 38–46. https://doi.org/10.1016/j.icarus.2013.04.011.

Head, J.W., Marchant, D.R., Dickson, J.L., Levy, J.S., Morgan, G.A., 2007. Slope Streaks in the Antarctic Dry Valleys: Characteristics, Candidate Formation Mechanisms, and

Implications for Slope Streak Formation in the Martian Environment. LPSC XXXVIII #1935.
Heyer, T., Erkeling, G., Hiesinger, H., Reiss, D., Luesebrink, D., Bernhardt, H., Jaumann, R., 2017. The Multi-temporal Database of Planetary Image Data (MUTED): a Tool to Support the Identification of Surface Changes on Mars. LPSC XLVIII #1019.
James, P.B., Thomas, P.C., Malin, M.C., 2010. Variability of the south polar cap of Mars in Mars years 28 and 29. Icarus 208, 82–85. https://doi.org/10.1016/j.icarus.2010.02.007.
James, P.B., Briggs, G., Barnes, J., Spruck, A., 1979. Seasonal recession of Mars' south polar cap as seen by Viking. J. Geophys. Res. 84, 2889–2922. https://doi.org/10.1029/JB084iB06p02889.
Jaret, S.J., Clevy, J.R., 2007. Distribution of Dark Slope Streaks in and Around Schiaparelli Impact Basin, Mars. LPSC XXXVIII #1973.
Jaumann, R., Neukum, G., Behnke, T., Duxbury, T.C., Eichentopf, K., Flohrer, J., Gasselt, S. v., Giese, B., Gwinner, K., Hauber, E., Hoffmann, H., Hoffmeister, A., Köhler, U., Matz, K.D., McCord, T.B., Mertens, V., Oberst, J., Pischel, R., Reiss, D., Ress, E., Roatsch, T., Saiger, P., Scholten, F., Schwarz, G., Stephan, K., Wählisch, M., 2007. The high-resolution stereo camera (HRSC) experiment on Mars Express: instrument aspects and experiment conduct from interplanetary cruise through the nominal mission. Planet. Space Sci. 55, 928–952. https://doi.org/10.1016/j.pss.2006.12.003.
Jaumann, R., Tirsch, D., Hauber, E., Ansan, V., Di Achille, G., Erkeling, G., Fueten, F., Head, J., Kleinhans, M.G., Mangold, N., Michael, G.G., Neukum, G., Pacifici, A., Platz, T., Pondrelli, M., Raack, J., Reiss, D., Williams, D.A., Adeli, S., Baratoux, D., De Villiers, G., Foing, B., Gupta, S., Gwinner, K., Hiesinger, H., Hoffmann, H., Deit, L., Le, Marinangeli, L., Matz, K.D., Mertens, V., Muller, J.P., Pasckert, J.H., Roatsch, T., Rossi, A.P., Scholten, F., Sowe, M., Voigt, J., Warner, N., 2015. Quantifying geological processes on Mars - results of the high resolution stereo camera (HRSC) on Mars express. Planet. Space Sci. 112, 53–97. https://doi.org/10.1016/j.pss.2014.11.029.
Kirk, R.L., Becker, K., Cook, D., Hare, T., Howington-Kraus, E., Isbell, C., Lee, E.M., Rosanova, T., Soderblom, L., Sucharski, T., Thompson, K., Davies, M., Colvin, T., Parker, T., 1999. Mars DIM: the Next Generation. LPSC XXX #1849.
Kreslavsky, M.A., Head, J.W., 2009. Slope streaks on Mars: a new "wet" mechanism. Icarus 201, 517–527. https://doi.org/10.1016/j.icarus.2009.01.026.
Levinthal, E.C., Green, W.B., Cutts, J.A., Jahelka, E.D., Johansen, R.A., Sander, M.J., Seidman, J.B., Young, A.T., Soderblom, L.A., 1973. Mariner 9-Image processing and products. Icarus 18, 75–101. https://doi.org/10.1016/0019-1035(73)90174-7.
Malin, M.C., Danielson, G.E., Ingersoll, A.P., Masursky, H., Veverka, J., Ravine, M.A., Soulanille, T.A., 1992. Mars observer camera. J. Geophys. Res. 97, 7699–7718. https://doi.org/10.1029/92je00340.
Malin, M.C., Edgett, K.S., Posiolova, L.V., McColley, S.M., Dobrea, E.Z.N., 2006. Present-day impact cratering rate and contemporary gully activity on mars. Science 314, 1573–1577. https://doi.org/10.1126/science.1135156 (80-.).
Malin, M.C., Bell, J.F., Cantor, B.A., Caplinger, M.A., Calvin, W.M., Clancy, R.T., Edgett, K.S., Edwards, L., Haberle, R.M., James, P.B., Lee, S.W., Ravine, M.A., Thomas, P.C., Wolff, M.J., 2007. Context camera investigation on board the mars reconnaissance orbiter. J. Geophys. Res. E Planets 112. https://doi.org/10.1029/2006JE002808.
Malin, M.C., Edgett, K.S., 2001. Mars global surveyor mars orbiter camera: interplanetary cruise through primary mission. J. Geophys. Res. 106, 23,429–23,570. https://doi.org/10.1029/2000JE001455.
Malin, M.C., Edgett, K.S., Cantor, B.A., Caplinger, M.A., Danielson, G.E., Jensen, E.H., Ravine, M.A., Sandoval, J.L., Supulver, K.D., 2010. An overview of the 1985-2006 Mars Orbiter Camera science investigation. Mars 5, 1–60.
McEwen, A.S., Ojha, L., Dundas, C.M., Mattson, S.S., Byrne, S., Wray, J.J., Cull, S.C., Murchie, S.L., Thomas, N., Gulick, V.C., 2011. Seasonal flows on warm martian slopes. Science 333, 740–743. https://doi.org/10.1126/science.1204816 (80-.).
McEwen, A.S., Eliason, E.M., Bergstrom, J.W., Bridges, N.T., Hansen, C.J., Delamere, W.A., Grant, J.A., Gulick, V.C., Herkenhoff, K.E., Keszthelyi, L., kirk, R.L., Mellon, M.T., Squyres, S.W., Thomas, N., Weitz, C.M., 2007. Mars reconnaissance orbiter's high resolution imaging science experiment (HiRISE). J. Geophys. Res. E Planets 112. https://doi.org/10.1029/2005JE002605.
Miyamoto, H., Dohm, J.M., Beyer, R.A., Baker, V.R., 2004. Fluid dynamical implications of anastomosing slope streaks on Mars. J. Geophys. Res. E Planets 109. https://doi.org/10.1029/2003JE002234.
Morris, E.C., 1982. Aureole deposits of the martian volcano Olympus Mons. J. Geophys. Res. 87, 1164. https://doi.org/10.1029/JB087iB02p01164.
Murchie, S., Arvidson, R., Bedini, P., Beisser, K., Bibring, J.P., Bishop, J., Boldt, J., Cavender, P., Choo, T., Clancy, R.T., Darlington, E.H., Des Marais, D., Espiritu, R., Fort, D., Green, R., Guinness, E., Hayes, J., Hash, C., Heffernan, K., Hemmler, J., Heyler, G., Humm, D., Hutcheson, J., Izenberg, N., Lee, R., Lees, J., Lohr, D., Malaret, E., Martin, T., McGovern, J.A., McGuire, P., Morris, R., Mustard, J., Pelkey, S., Rhodes, E., Robinson, M., Roush, T., Schaefer, E., Seagrave, G., Seelos, F., Silverglate, P., Slavney, S., Smith, M., Shyong, W.J., Strohbehn, K., Taylor, H., Thompson, P., Tossman, B., Wirzburger, M., Wolff, M., 2007. Compact connaissance imaging spectrometer for mars (CRISM) on mars reconnaissance orbiter (MRO). J. Geophys. Res. E Planets 112. https://doi.org/10.1029/2006JE002682.
Mushkin, A., Gillespie, A.R., Montgomery, D.R., Schreiber, B.C., Arvidson, R.E., 2010. Spectral constraints on the composition of low-albedo slope streaks in the Olympus Mons aureole. Geophys. Res. Lett. 37 https://doi.org/10.1029/2010GL044535.
Neukum, G., Jaumann, R., 2004. HRSC: The High Resolution Stereo Camera Of Mars Express. Eur. Sp. Agency, pp. 17–35. Special Publ. ESA SP.
Ojha, L., Wilhelm, M.B., Murchie, S.L., McEwen, A.S., Wray, J.J., Hanley, J., Massé, M., Chojnacki, M., 2015. Spectral evidence for hydrated salts in recurring slope lineae on Mars. Nat. Geosci. 8, 829–832. https://doi.org/10.1038/ngeo2546.
Piqueux, S., Christensen, P.R., 2008. Deposition of CO2 and erosion of the Martian south perennial cap between 1972 and 2004: implications for current climate change. J. Geophys. Res. E Planets 113. https://doi.org/10.1029/2007JE002969.
Piqueux, S., Kleinböhl, A., Hayne, P.O., Kass, D.M., Schofield, J.T., McCleese, D.J., 2015. Variability of the martian seasonal CO_2 cap extent over eight Mars years. Icarus 251, 164–180. https://doi.org/10.1016/j.icarus.2014.10.045.
Raack, J., Reiss, D., Appéré, T., Vincendon, M., Ruesch, O., Hiesinger, H., 2015. Present-day seasonal gully activity in a south polar pit (Sisyphi Cavi) on Mars. Icarus 251, 226–243. https://doi.org/10.1016/j.icarus.2014.03.040.
Reiss, D., Erkeling, G., Bauch, K.E., Hiesinger, H., 2010. Evidence for present day gully activity on the Russell crater dune field, Mars. Geophys. Res. Lett. 37 https://doi.org/10.1029/2009GL042192.
Reiss, D., Hoekzema, N.M., Stenzel, O.J., 2014a. Dust deflation by dust devils on Mars derived from optical depth measurements using the shadow method in HiRISE images. Planet. Space Sci. 93–94, 54–64. https://doi.org/10.1016/j.pss.2014.01.016.
Reiss, D., Spiga, A., Erkeling, G., 2014b. The horizontal motion of dust devils on Mars derived from CRISM and CTX/HiRISE observations. Icarus 227, 8–20. https://doi.org/10.1016/j.icarus.2013.08.028.
Reiss, D., Zanetti, M., Neukum, G., 2011. Multitemporal observations of identical active dust devils on mars with the high resolution stereo camera (HRSC) and mars orbiter camera (MOC). Icarus 215, 358–369. https://doi.org/10.1016/j.icarus.2011.06.011.
Reiss, D., Lorenz, R.D., 2016. Dust devil track survey at Elysium Planitia, Mars: implications for the InSight landing sites. Icarus. https://doi.org/10.1016/j.icarus.2015.11.012.
Russell, P., Thomas, N., Byrne, S., Herkenhoff, K., Fishbaugh, K., Bridges, N., Okubo, C., Milazzo, M., Daubar, I., Hansen, C., McEwen, A.S., 2008. Seasonally active frost-dust avalanches on a north polar scarp of Mars captured by HiRISE. Geophys. Res. Lett. 35 https://doi.org/10.1029/2008GL035790.
Sagan, C., Veverka, J., Fox, P., Dubisch, R., Lederberg, J., Levinthal, E., Quam, L., Tucker, R., Pollack, J.B., Smith, B.A., 1972. Variable features on Mars: preliminary mariner 9 television results. Icarus 17, 346–372. https://doi.org/10.1016/0019-1035(72)90005-X.
Schorghofer, N., King, C.M., 2011. Sporadic formation of slope streaks on Mars. Icarus 216, 159–168. https://doi.org/10.1016/j.icarus.2011.08.028.
Sidiropoulos, P., Muller, J.P., 2015. On the status of orbital high-resolution repeat imaging of Mars for the observation of dynamic surface processes. Planet. Space Sci. 117, 207–222. https://doi.org/10.1016/j.pss.2015.06.017.
Smith, D.E., Zuber, M.T., Frey, H.V., Garvin, J.B., Head, J.W., Muhleman, D.O., Pettengill, G.H., Phillips, R.J., Solomon, S.C., Zwally, H.J., Banerdt, W.B., Duxbury, T.C., Golombek, M.P., Lemoine, F.G., Neumann, G.A., Rowlands, D.D., Aharonson, O., Ford, P.G., Ivanov, A.B., Johnson, C.L., McGovern, P.J., Abshire, J.B., Afzal, R.S., Sun, X., 2001. Mars orbiter laser altimeter: experiment summary after the first year of global mapping of mars. J. Geophys. Res. Planets 106, 23689–23722. https://doi.org/10.1029/2000JE001364.
Soffen, G.A., Snyder, C.W., 1976. The first Viking mission to Mars. Am. Assoc. Adv. Sci. 193, 759–766. https://doi.org/10.1126/science.193.4255.759.
Stanzel, C., Pätzold, M., Greeley, R., Hauber, E., Neukum, G., 2006. Dust devils on mars observed by the high resolution stereo camera. Geophys. Res. Lett. 33 https://doi.org/10.1029/2006GL025816.
Stanzel, C., Pätzold, M., Williams, D.A., Whelley, P.L., Greeley, R., Neukum, G., 2008. Dust devil speeds, directions of motion and general characteristics observed by the Mars Express high resolution stereo camera. the HRSC Co-Investigator Team Icarus 197, 39–51. https://doi.org/10.1016/j.icarus.2008.04.017.
Sullivan, R., Thomas, P., Veverka, J., Malin, M.C., Edgett, K.S., 2001. Mass movement slope streaks imaged by the Mars orbiter camera. J. Geophys. Res. E Planets 106, 23607–23633. https://doi.org/10.1029/2000JE001296.
Tanaka, K.L., Skinner, J.A., Dohm, J.M., Irwin III, R.P., Kolb, E.J., Fortezzo, C.M., Platz, T., Michael, G.G., Hare, T.M., 2014. Geologic Map of Mars. Scientific Investigations Map, Reston, VA. https://doi.org/10.3133/sim3292.
Thomas, P.C., James, P.B., Calvin, W.M., Haberle, R., Malin, M.C., 2009. Residual south polar cap of Mars: stratigraphy, history, and implications of recent changes. Icarus 203, 352–375. https://doi.org/10.1016/j.icarus.2009.05.014.
van Gasselt, S., Reiss, D., Thorpe, A.K., Neukum, G., 2005. Seasonal variations of polygonal thermal contraction crack patterns in a south polar trough. Mars. J. Geophys. Res. E Planets 110, 1–15. https://doi.org/10.1029/2004JE002385.
Veverka, J., Sagan, C., Quam, L., Tucker, R., Eross, B., 1974. Variable features on mars III: comparison of mariner 1969 and mariner 1971 photography. Icarus 21, 317–368. https://doi.org/10.1016/0019-1035(74)90046-3.
Vincendon, M., Audouard, J., Altieri, F., Ody, A., 2015. Mars Express measurements of surface albedo changes over 2004-2010. Icarus 251, 145–163. https://doi.org/10.1016/j.icarus.2014.10.029.
Zurek, R.W., Martin, L.J., 1993. Interannual variability of planet-encircling dust storms on Mars. J. Geophys. Res. 98, 3247. https://doi.org/10.1029/92JE02936.